Process induced modulation of domain orientations during WS_2 epitaxy by metal-organic chemical vapor deposition on sapphire

Joris Verdin[1,2,], Henry Medina Silva[1,*], Ankit Nalin Mehta[1], Iryna Kandybka[1,2], Benjamin Groven[1], Pawan Kumar[1], Serkan Koylan[1,3], Stefanie Sergeant[1],Paola Favia[1], Pierre Morin[1], Annelies Delabie[1,2,*]*

1. Imec, Kapeldreef 75, Leuven, 3001, Belgium
2. Department of Chemistry, KU Leuven, Celestijnenlaan 200F, Leuven, 3001, Belgium
3. Department of Physics and Astronomy, KU Leuven, Celestijnenlaan 200D, Leuven, 3001, Belgium

E-mail: Joris.Verdin@imec.be, Henry.MedinaSilva@imec.be, Annelies.Delabie@imec.be

KEYWORDS: two-dimensional (2D) materials, nanoelectronics, chemical vapor deposition, transition metal dichalcogenides, Van der Waals epitaxy, sapphire template, tungsten disulfide

ABSTRACT:

Single monolayers (MLs) of transition metal dichalcogenides (TMDs) like molybdenum disulfide (MoS_2) and tungsten disulfide (WS_2) are promising semiconductors for next-generation logic devices, photodetectors, and light-emitting diodes. Applications require industry-relevant deposition techniques that form large monocrystalline TMD domains with low defect density. In this work, we study the growth of WS_2 by metal-organic chemical vapor deposition on c-plane sapphire substrates at different temperatures. We investigate the growth phenomena during the initial stages before ML formation and apply the obtained knowledge to design an optimized deposition process. High deposition temperatures (1000 °C) yield a high degree of in-plane crystal orientation but give rise to co-deposition of WS_2 and tungsten, presumably due to the fast desorption of sulfur species. The preferred WS_2 domain orientation can be modulated by the process: WS_2 deposition at 850 °C followed by annealing of WS_2 crystals in H_2S at 1000 °C results mainly in step-edge guided domains, whereas crystal lattice guided domains are predominant during subsequent deposition at 1000 °C. The optimized three-step process results in a preferential formation of 0 ° and 60 ° oriented domains in the closed WS_2 ML, with less than 2 % of crystals with different orientations. These presented insights can be used to modulate and optimize the WS_2 structure further towards monocrystalline monolayers.

INTRODUCTION:

TMDs are a versatile group of materials with a wide range of possible applications.[1–3] Two-dimensional (2D) monolayers of molybdenum disulfide (MoS_2) and tungsten disulfide (WS_2) have the potential to act as ultimately scaled semiconductor channel in future advanced field-effect transistors if prepared in ML form.[4–6] Furthermore, WS_2 has potential optical applications such as absorbing semiconducting layer in photodetectors[7–9] or emission layer in light-emitting diodes.[8-10] For these applications, the TMD layer should ideally be monocrystalline, as grain boundaries can induce scattering of charge carriers or modify the optical properties.[11–15] An often-considered route to achieve monocrystalline TMDs is to grow crystal domains epitaxially on a monocrystalline template and merge the individual domains into one continuous phase. *C*-plane or (0001) sapphire (α-Al_2O_3) is studied extensively as a substrate for epitaxy due to the widespread availability, high chemical and thermal stability, hexagonal symmetry, and low lattice mismatch with MoS_2 and WS_2.[16] Two unit cells of *c*-plane sapphire ($a_{\alpha\text{-}Al2O3}$ = 4.760 Å) overlap almost perfectly with three unit cells of the semiconducting 2H-MoS_2 ($a_{2H\text{-}MoS2}$ = 3.160 Å) and 2H-WS_2 ($a_{2H\text{-}WS2}$ = 3.153 Å) phases, creating the possibility to achieve systems with low lattice mismatch upon formation of a commensurate superstructure.[16,17] Such superstructures can be formed as the substrate and newly grown TMD material are held together only by Van der Waals forces and not by covalent bonds. Still, the generated domains can exhibit different in-plane orientations. Most experimental studies with (0001) sapphire observe both parallel and antiparallel orientations of the $[1\bar{2}10]$ axis of the sapphire substrate and the MoS_2 (or WS_2) crystals.[16–19] Crystal domains with these specific in-plane orientations are often referred to as 0 ° or 60 ° oriented crystals, respectively. The 0 ° or 60 ° oriented crystals have been considered as the energetically most favorable options on (0001) sapphire.[18,20]

TMDs can be synthesized using various techniques, but not all procedures are suitable for the preparation of wafer-scale MoS_2 or WS_2 in an industrial setting. Chemical vapor deposition (CVD) is an industry-relevant deposition method yielding highly reproducible TMD MLs with low defect density.[21] However, it remains challenging to prepare large area monocrystalline domains, amongst others due to the energetic equivalence of the 0 ° and 60 ° oriented crystals generated during epitaxy on (0001) sapphire. Merging two such crystals can generate mirror twin grain boundaries, but research about the effect of these features on material properties has not reached a consensus yet (both no impact[18,22] and material degradation reported).[23,24] A potential approach to induce unidirectional crystal growth is performing the deposition on (0001) sapphire surfaces with minor, deliberately introduced off-cut angles towards an alternative crystallographic axis. The resulting stepped surface structure may guide the MoS_2 and WS_2 crystal growth towards one preferred orientation, but the mechanism and how the template guides the crystal orientation is under debate.[17–19,25–28] The roles of the surface topography and crystal lattice of the growth substrate on the growth of MoS_2 have been extensively investigated, which enabled close to unidirectional growth. Still, the growth conditions, e.g., deposition temperature, flow rates, partial pressures of precursors and co-reactants, and seeding steps prior to TMD deposition, also play an important role.[25,29–31] The role of the temperature has been investigated for MoS_2 and WSe_2,[28,32] but WS_2 remained somewhat overlooked until now, despite its great promise in terms of charge carrier mobility. Chubarov et al. studied WS_2 deposition at variable temperatures with intermediate annealing and demonstrated that temperature selection is crucial to promote growth conditions yielding unidirectional WS_2 crystals.[17] Nevertheless, selecting an optimal temperature remains not trivial, as one should consider both the growth mechanism of the growing TMD phase as well as the reconstruction of the template at high temperatures. This can be illustrated by the fact that

temperatures ≥ 1000 °C generally result in high quality TMD epitaxy, but substrates like sapphire undergo surface reconstruction at this temperature.[17,21,33–35] The parallel alignment of step-edges is lost as a result of this reconstruction, which could affect the degree of in-plane TMD crystal orientation.[17] On the other hand, the high mobility of surface adspecies during reconstruction could be beneficial for epitaxy. Clearly, a detailed understanding of the influence of temperature on the WS_2 growth mechanism is still missing.

The objective of this study is to acquire insight into the growth mechanisms of WS_2 metal-organic chemical vapor deposition (MOCVD) using hydrogen sulfide (H_2S) and tungsten hexacarbonyl ($W(CO)_6$) precursors on (0001) sapphire substrates. We investigate the WS_2 structure and in-plane orientation of WS_2 domains for deposition at two different temperatures (850 and 1000 °C), as well as the impact of intermediate annealing in H_2S. The substrate of choice is (0001) sapphire with a 1 ° off-cut towards the $[1\bar{2}10]$ axis, as this allows us to distinguish step-edge guided and crystal lattice guided epitaxy: step-edge guided epitaxy leads to 30 and 90 ° orientation of domains, whereas crystal lattice guided epitaxy leads to 0 and 60 ° orientation of domains. The obtained insights are combined in an optimized deposition process that yields a more pure monocrystalline WS_2 ML.

METHODS:

MOCVD

We perform WS_2 depositions in a custom-built, industrially compatible 200 mm CVD reactor installed on a POLYGON8200 (**Figure S1**). High purity H_2S, N_2 and Ar are obtained from gas cylinders provided by Air Liquide. $W(CO)_6$ is vaporized in a metallic canister (Air Liquide) held at a pressure of 900 mbar and temperature of 35 °C by passing an Ar flow through it. We place two 2-inch (0001) sapphire wafers with a 1 ° off-cut angle towards the $[1\bar{2}10]$ axis (Roditi

International Corporation) on a 200 mm SiC-coated Si carrier wafer equipped with appropriate pockets (**Figure S1**). The carrier wafer is then placed on a continuously rotating disc in the CVD reactor. All wafer handling is performed in a N_2 ambient. Prior to WS_2 deposition, the CVD chamber is loaded with the carrier wafer and subsequently purged with a N_2 flow. We use N_2 as carrier gas, the total gas flow rate equals 20 slm and the total reactor pressure 75 Torr during all processes. Initially, the temperature is increased to 850 or 1000 °C. Once the temperature stabilizes, H_2S (2.06×10^{-1} Torr) and $W(CO)_6$ (5.52×10^{-6} Torr) are inserted into the reactor. The deposition is performed for 2, 5, 10, 20, 30, 200 or 300 min, after which both the $W(CO)_6$ flow and the heating is stopped. Every sample is prepared in duplicate, and both obtained sapphire wafers with deposited WS_2 are used for subsequent characterization.

Atomic force microscopy (AFM)

The topography of the sapphire surface and the formed features are characterized by AFM using a Dimension Icon PR system from Bruker in PeakForce-Quantitative Nanomechanical Mapping mode equipped with a HQ-NSC19/AlBS tip. Afterwards, the obtained data is analyzed using the Gwyddion software. All numerical data presented in this work is obtained by analyzing two samples for each condition (on two locations per sample).

Transmission electron microscopy (TEM)

Prior to TEM analysis, we transfer closed WS_2 MLs from the sapphire surface onto a TEM grid using the method reported by Nalin Mehta et al.[36] Plan-view TEM is carried out in a FEI Tecnai F30 transmission electron microscope operated at 200 kV. We acquire both bright field (BF)- and dark field (DF)-TEM images of our samples in a grid pattern. The smallest objective aperture (10 μm) is used to select the transmitted beam and one of the first order $\{10\bar{1}0\}$ diffracted beam of WS_2. While the BF-TEM images provide information about the layer thickness, the DF-TEM

images contain contrast related to the grain orientation. Grains rotated by 60 ° relative to the predominant orientation can be differentiated due to the intensity asymmetry of diffraction peaks stemming from the lack of centrosymmetry in a single layer of WS_2.[52] Moreover, grains oriented with a high angle misorientation which we refer to as intermediate domains appear dark as the electrons diffracted from them are excluded in the DF image formation. However, it is worth noting that when the misoriented domains in the material are separated by small misorientations, the objective aperture, due to its finite width, allows electrons diffracted from more than one specific orientation when forming the image. As a result, domains with small misorientations cannot be differentiated and the fraction of oriented domains in such a sample can be exaggerated. In each mode (BF/DF), 100 images are acquired in a 10 x 10 grid pattern with a certain overlap at 3900 kx magnification. The images are then montaged with a scale-invariant feature transform algorithm in ImageJ. The DF-TEM images are segmented using a custom python script wherein the BF-TEM image is used to mask the carbon support as well as the multi-layered regions prior to image segmentation and percentage estimation of orientations (**Figure S2**). In addition, we characterize features further using energy dispersive X-ray spectroscopy (EDX) combined with high-resolution scanning TEM (HR-STEM) on a Thermo-Fisher Titan G^2 60-300 operated at 200 kV.

Rutherford backscattering spectrometry (RBS)

RBS measurements are executed in a random rotation mode using 1.5 MeV He^+ ions from a 6SDH tandem accelerator (National Electrostatics Corporation) connected to an Alphatross ion source. The experimental end-station is a 5-axis goniometer developed at the Forshungszentrum Jülich. The angle between the beam and the normal on the samples is set to 11 °. The solid angle of the PIPS detector is 0.42 msr, the scattering angle was 170 °. The beam spot is confined to

1x1 mm^2. More details on the experimental setup are available in the publication of Meersschaut et al.[37] In house developed analysis software is used for the fitting to derive the tungsten and sulfur areal density from the spectra.

Grazing incidence in-plane X-ray diffraction (GIIXRD)

We perform GIIXRD measurements with a Malvern Panalytical X'PERT Pro diffractometer combined with PIXcel detector and Ni filter. X-rays are generated by applying 40 kV acceleration voltage and 45 mA filament current to an X-ray tube with copper anode. The setup also contains a 0.7 mm divergence slit placed in between the X-ray source and sample stage. We calibrate the setup by placing the X-ray source, sample stage and detector within one plane and measuring Bragg diffraction of the $(1\bar{2}10)$ sapphire planes. The sample orientation (φ) displaying maximal diffraction intensity is in subsequent measurements referred to as φ = 0 °. Next, we adjust 2θ to 58.417 ° and φ to 0 ° before measuring diffraction while varying the angle of incidence (ω) between -1 and 1 °. The ω angle yielding maximal diffraction is used in all following measurements. We evaluate the in-plane WS_2 crystal orientation by rotating the sample around the φ-axis from -95 to 95 °, in steps of 0.04 °.

Raman/photoluminescence spectroscopy

Raman spectroscopy system (Horiba-LabRAM) is used to investigate the characteristics of phonon vibrations belonging to 2D WS_2 MLs. We used a 532 nm laser as a source of excitation, optimal excitation power (ND filter 1%) to not create any local heating or defects, 50 x large working distance objective lens, 120 sec acquisition time per spectral window, and 1800 grating lines, which provide very high spectral resolution. Photoluminescence (PL) spectroscopy is also

performed on the same Horiba-LabRAM set-up utilizing a 532nm laser source, 1% excitation power, 50x LWD objective and 20 sec acquisition time per spectral window with 600 grating lines.

RESULTS AND DISCUSSION:

Deposition at 850 °C

To enable the design of optimized MOCVD processes for monocrystalline WS_2 MLs, we investigate the WS_2 growth behavior at different deposition temperatures. Our study starts with experiments at a deposition temperature of 850 °C (**Figure 1a**). During the early stages of growth at 850 °C in sulfur (S)-rich conditions, we observe one material phase with a characteristic height of ~0.8 nm, corresponding to single WS_2 ML, as assessed by AFM (**Figure 1b**). Triangular-shaped WS_2 crystals are formed, in agreement with literature.[38] After 20 min of deposition, the average lateral crystal area equals 9.6 x 10^2 nm^2. In addition, AFM demonstrates that a significant part of the domains has an irregular shape. To gain insight into the growth mechanism, we analyze the amount of deposited material, crystal size, and crystal number density in the early deposition process before coalescence and WS_2 layer closure. The areal density of tungsten (W, assessed by RBS) increases linearly as a function of the deposition time, with a growth rate of 4.2 x 10^{12} W atoms/min·cm^2 (corresponding to a growth rate of 0.004 WS_2 ML/min, **Figure S3**). While the amount of deposited material increases linearly, the number density of WS_2 crystals reaches a steady value (~ 1.4 x 10^2 μm^{-2}) between 5 and 30 min (AFM, **Figure S4** and **Figure S5**). Thus, in this steady state regime, the crystals grow laterally in size. The particle size distributions (PSDs) support this observation, as we note an increase in the lateral areas for longer deposition times (**Figure S6a**). In addition, the PSD changes from bimodal to unimodal after 10 min of deposition.

The observations during the early nucleation stages may be caused by a complex interplay of different elementary processes.[39] The metal precursor fully decomposes at a temperature of 850 °C

($W(CO)_6$ dissociates at temperatures above 350 °C).[40] W atoms and S species adsorb on the surface and the W adspecies are subsequently sulfurized. In addition, newly arriving W and S adspecies and small WS_2 nuclei may diffuse over the surface. During this adsorption and diffusion regime, the crystal number density typically increases. Our observations suggest this occurs for deposition times shorter than 2 min. Crystal aggregation becomes more important when nuclei reach a specific number density, leading to a steady state with a constant number of islands where adsorption, diffusion, and aggregation of species are in equilibrium (2 to 30 min).[39] Furthermore, ripening may also occur between WS_2 nuclei, which may explain the large presence of small crystals (≤ 100 nm^2) during the first 10 min and their absence for longer deposition times.

To better understand the formation of the WS_2 ML and the orientation of domains, we analyze the in-plane crystal orientation. The irregular shape of the WS_2 crystals formed during the first 30 min of deposition makes it impossible to assess the domain orientation by AFM. Instead, we use TEM to evaluate the in-plane orientation of domains in a closed ML (photograph provided in **Figure S7**). For the selected sample, the areal density of W corresponds to a full ML (1.13×10^{15} atoms/cm^2, RBS, **Figure S8**), and the Raman scattering is consistent with data for different vibrational modes of a single WS_2 MLs reported in literature (**Figure S9**).[41,42] DF-TEM montage segmentation reveals that this ML consists of 44.0, 36.8 and 19.2 % of 0 °, 60 ° and intermediate oriented domains, respectively (**Figure 1c**, **Figure 1d** and **Figure S2).** Larger size and enlarged DF-TEM montages are provided in **Figures S10-S15**. The 0 and 60 ° crystal orientations correspond to the lowest energy and are commonly observed.[18,20] The existence of domains with different orientations implies that grain boundaries are present, which can affect/degrade the material properties of the WS_2 film. Therefore, one should attempt to limit the formation of these features.[24]

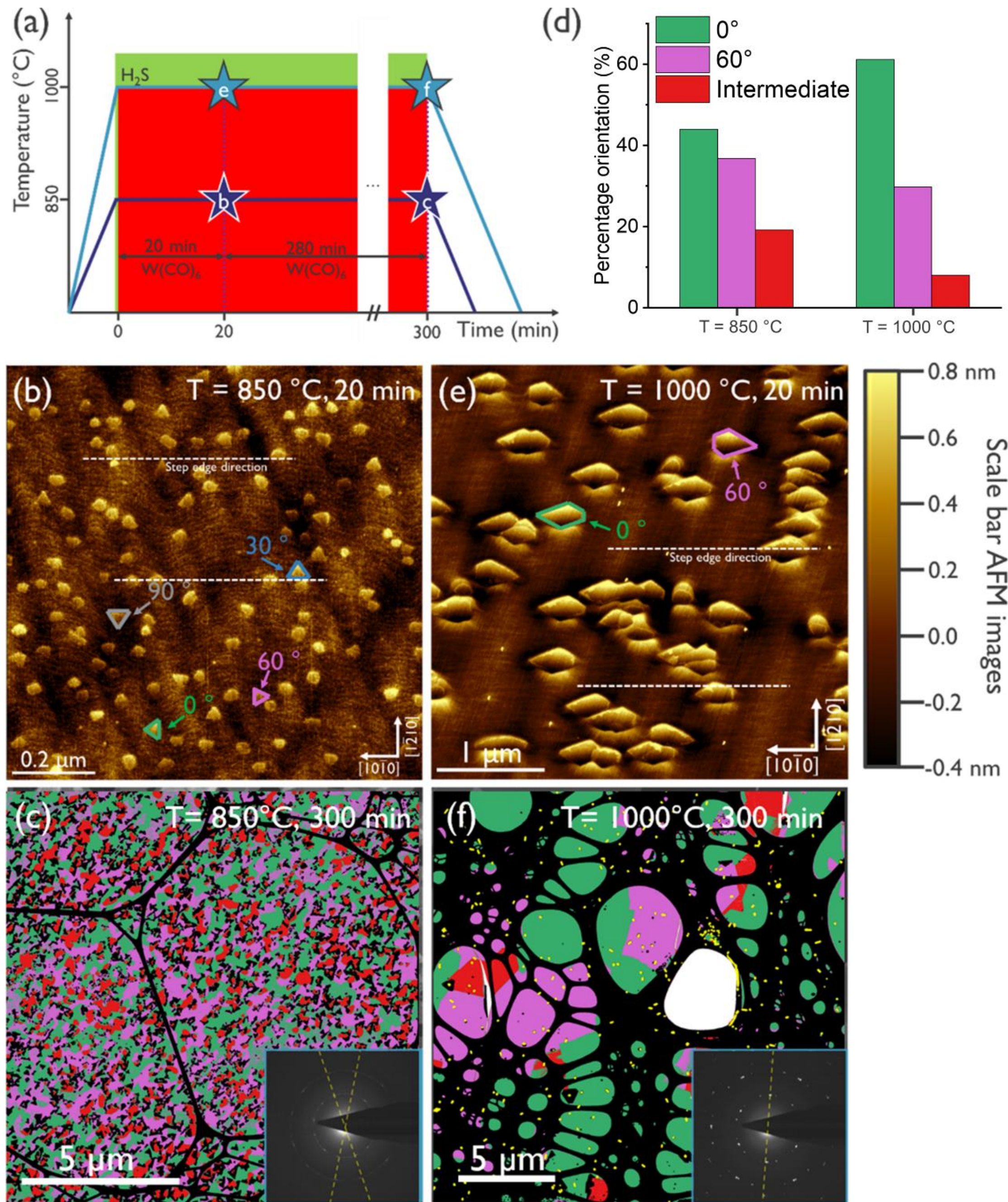

Figure 1: ***(a)*** *Schematic representation deposition process at constant deposition temperatures, insertion of* H_2S *and* $W(CO)_6$ *precursors is indicated by green and red, respectively. The deposition temperature for different samples is indicated by blue lines.* ***(b)*** *AFM topography map after 20 min of* WS_2 *deposition at 850 °C.* WS_2 *crystals with one facet parallel to the* $\langle 1\bar{2}10 \rangle$ *axis are referred to as 0 ° oriented (green) or 60 ° oriented (pink). 30 ° and 90 ° oriented islands are indicated with blue and grey, respectively. The white dashed line indicates a step-edge.* ***(c)*** *Segmented DF-TEM montage of a closed ML formed after 300 min of* WS_2 *deposition at 850 °C, with the corresponding electron diffraction pattern (ED) in the inset. The yellow dashed lines indicate the predominant orientations.* ***(d)*** *Fractions of 0 °,60 ° and intermediate oriented domains in MLs obtained after 300 min of* WS_2 *deposition, with a deposition temperature of either 850 or 1000 °C (obtained by segmentation of DF-TEM montage).* ***(e)*** *AFM topography map after 20 min of* WS_2 *deposition at 1000 °C. The observed diamond-like crystals are the result of anisotropic diffusion over the sapphire substrate.* ***(f)*** *Segmented DF-TEM montage of a closed ML formed after 300 min of* WS_2 *deposition at 1000 °C, with the corresponding ED pattern in the inset. The colors in the segmented DF-TEM montages in (c) and (f) correspond to 0 ° (green) or 60 ° (pink) and intermediate orientations (red), in analogy with (b). Additional colors in (f): yellow represents metallic W and white corresponds to a hole where layer was locally delaminated.*

Deposition at 1000 °C

We attempt to limit the formation of intermediate oriented crystals by increasing the deposition temperature to 1000 °C, since the quality of epitaxy can improve at higher temperatures. The growth rate is similar for deposition at 1000 °C and 850 °C, i.e., 0.004 ML/min (RBS, **Figure S3**). However, the morphology is different. For deposition at 1000 °C, we observe two types of features during the early nucleation stage in the AFM topography maps: triangular- and diamond-like crystals with a height of ~0.8 nm (WS_2), and rounded structures with higher height (> 5 nm, **Figure 1e** and **Figure S16**). The number density of WS_2 crystals is constant around 2.3 μm^{-2} between 5 and 20 min of deposition (850 °C deposition: 1.4×10^2 μm^{-2}, **Figure S4**). The PSDs of these islands reveal an increase in the lateral area of the crystals with increasing deposition time (**Figure S6b**). After 20 min of deposition at 1000 °C, the average lateral WS_2 crystal area equals 5.1×10^4 nm^2 (compare to 6.9×10^2 nm^2 after identical deposition time at 850 °C). DF-TEM indicates that the closed ML consists of 61.2 % 0 ° oriented crystals and 29.8 % 60 ° oriented domains (**Figure 1d, Figure 1f** and **Figure S2**). The remaining 8.0 % can be attributed to intermediate oriented domains.

We perform additional characterization to identify the features with circular lateral shape. These particles have a hemi-ellipsoidal three-dimensional shape during the early nucleation stage, as indicated by AFM topography maps (**Figure S17**). These hemi-ellipsoidal clusters grow between 5 and 200 min of deposition, as their average height and lateral radius increase from 6 to 21 nm and from 11 to 29 nm, respectively (**Figure 2a**). Initially, the number density of these clusters is three times higher as compared to the WS_2 domains density (after 2 min), but it rapidly decreases upon prolonging the deposition process (-82 % after 10 min, -98% after 200 min, **Figure 2a**). Despite this quick reduction in the number of clusters, we keep observing these clusters in the later

stages of growth, even after closure of the ML. In the closed ML, acquired after 300 min of deposition, we observe rod-like features by TEM (yellow features in the images in **Figure 1f**). The rod-like features mainly consist of W, with small amounts of oxygen and almost no S, as indicated by EDX during scanning TEM (**Figure 2b-e**). We observe a lattice fringe of 0.23 nm when analyzing the clusters with HR-STEM (**Figure 2f**). This value is close to the spacing between the (110)-planes of metallic W (0.22 nm as reported in literature).[43] The fact that we observe metallic W co-deposition when increasing the deposition temperature is consistent with the finding of Eichfeld et al.[44], who observed the formation of Se-deficient WSe_2 domains when increasing the deposition temperature from 800 °C to 900 °C.

The co-deposition of W clusters during WS_2 MOCVD at 1000 °C may be related to the high desorption rate of S species. Due to the high vapor pressure of S species, S adspecies inevitably desorb from the surface at all applied deposition temperatures. In contrast, the vapor pressure of W is multiple orders of magnitude lower. W is expected to desorb at a slower rate and the average lifetime of W adspecies on the surface is most likely longer than that of S adspecies.[17,32] Note that several factors determine the lifetime of adspecies, including interactions with the substrate, adsorption/desorption equilibria and the rates of surface reactions, surface diffusion, and adspecies aggregation.[45] In order to generate sufficient S adspecies during WS_2 MOCVD, we supply an excess of H_2S compared to the $W(CO)_6$ precursor. Still, the differences in vapor pressures of S and W species become larger at higher temperatures (**Figure 2g**).[46,47] Therefore, the ratio of S versus W adspecies on the surface reduces at higher temperatures. Because the relative concentration of S adspecies on the surface is lower at 1000 °C, the equilibrium could shift. This is consistent with the formation of metallic W clusters in addition to WS_2 crystals. Alternatively, gaseous W atoms may also aggregate in the gas phase and adsorb as a cluster onto the surface. S adspecies may

sulfurize these metallic clusters to form WS_2, but this reaction becomes less likely on surfaces with reduced presence of S adspecies. A graphical representation of the gas-phase and surface processes of W and S species is provided in **Figure 3**. Irrespective of the origin of these clusters, the lower S versus W ratio on the growth surface at higher deposition temperatures will favor the growth of W particles. Lower $W(CO)_6$ or higher H_2S flows during deposition may eliminate the formation of these clusters. However, surface reconstruction of the sapphire substrate occurs faster in S-rich conditions, and this may affect the WS_2 growth mode and final domain orientation. Alternatively, deposition at temperatures between 850 and 1000 °C may also yield WS_2 MLs without metallic W particles, although deposition with the same process at 950 °C still displays the presence of these clusters (**Figure S18**). Furthermore, influencing the surface termination using substrate annealing prior to WS_2 deposition can also lead to changes in the rate of metallic W formation (**Figure S19, Figure S20, Table S1 and Table S2**). Preliminary preannealing experiments resulted in more rather than less metallic W clusters. A detailed study on preannealing of sapphire substrate is however outside the scope of this work.

We also observe other unreported details of the WS_2 growth mechanism at 1000 °C. Interestingly, the TMD crystal shape evolves from triangular- to diamond-like between 5 and 20 min (**Figure S16**). This shape evolution may be the result of anisotropic crystal growth, as recently described for MoS_2 MOCVD with similar precursors and process conditions.[28] The observed steady-state and unimodal PSDs may suggest that WS_2 growth at 1000 °C proceeds by diffusion and aggregation of adspecies and/or crystals. The formation rate of new crystals is, in this case, similar to the crystal aggregation rate. Note that ripening of domains cannot be excluded based on the presented observations. The role of the co-deposited W clusters in the growth mechanism should not be neglected. As mentioned, hemi-ellipsoidal W clusters gradually grow over time, but

their number density quickly decreases after 10 min (**Figure 2a**). This sharp reduction may be the result of ripening. As few W clusters grow even until closure of the WS_2 ML, their ripening process likely affects the WS_2 crystal growth, as the WS_2 domains cover a far greater percentage of the surface. The shape evolution of co-deposited W clusters (from hemi-ellipsoidal to rod-like) is likely related to delayed crystallization. Several groups report crystallization of amorphous material during ALD and CVD processes when the deposited features reach specific dimensions.[48–50]

Increasing the deposition temperature from 850 to 1000 °C promotes a higher quality epitaxy, as indicated by the lower percentage of intermediate oriented domains (**Figure 1d**). This trend may be caused by WS_2 crystals having more energy to orient to the energetically most favorable orientation at higher temperature. Similarly, more adspecies can reach the most favorable positions on the surface when applying higher temperatures. Interestingly, the increasing degree of epitaxial in-plane orientation with temperature is not in line with the findings of Chubarov and coworkers.[17] The differences between the reported observations and this study may be related to the experimental conditions, such as sapphire preparation, carrier gases, and precursor flows (comparison experimental conditions provided in **Table S3**).

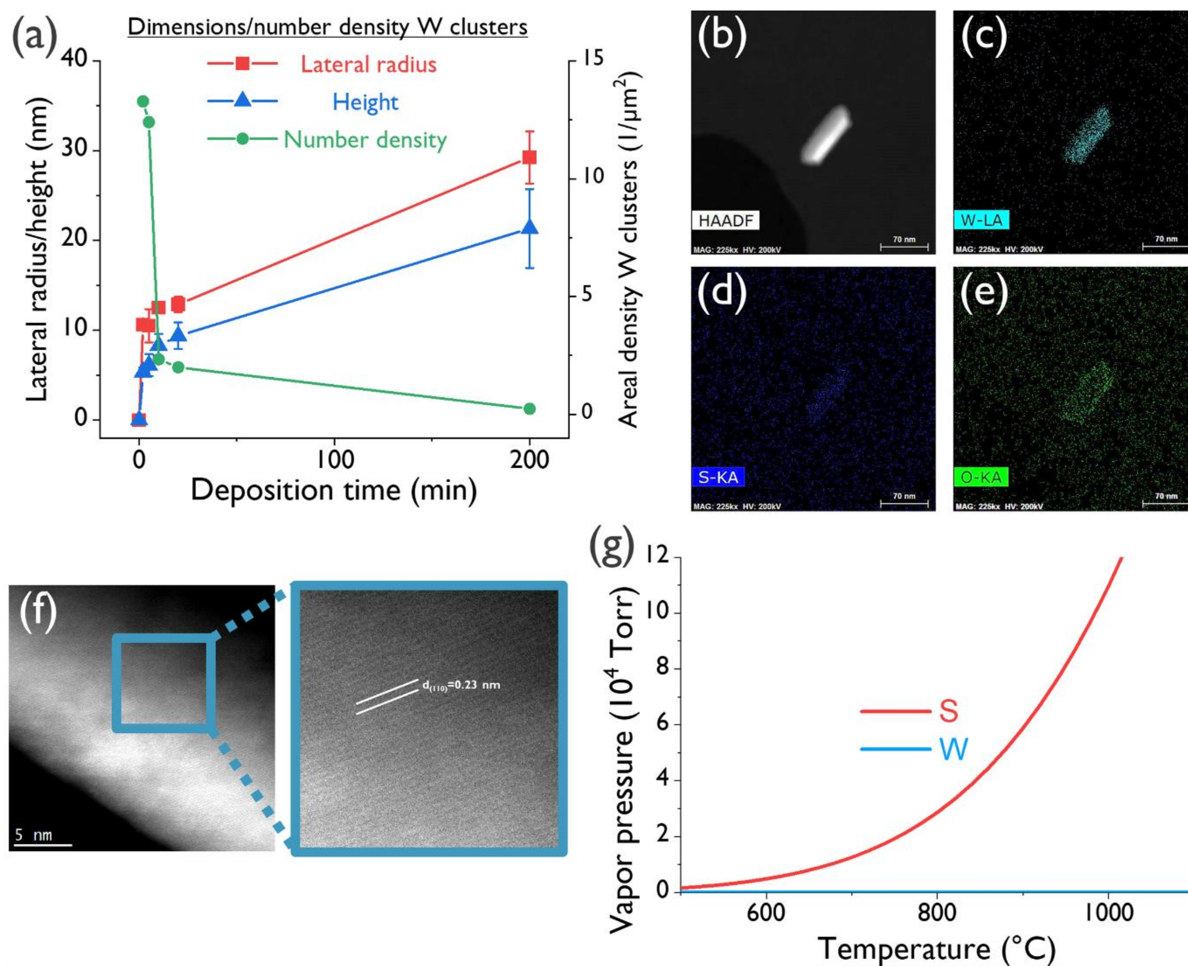

Figure 2: ***(a)*** *Evolution number density, height and lateral radius of metallic W clusters during deposition at 1000 °C.* ***(b)*** *High-angle annular dark-field STEM image of a metallic W particle. The same particle is characterized by measuring the emission of W-*L_α ***(c)****, S-*K_α ***(d)*** *and oxygen-*K_α *X-rays* ***(e)****.* ***(f)*** *HR-STEM analysis of a metallic W nanoparticle, indicating a lattice fringe close to the value reported for metallic W.*[43] ***(g)*** *Vapor pressure of elemental S and W as a function of temperature.*

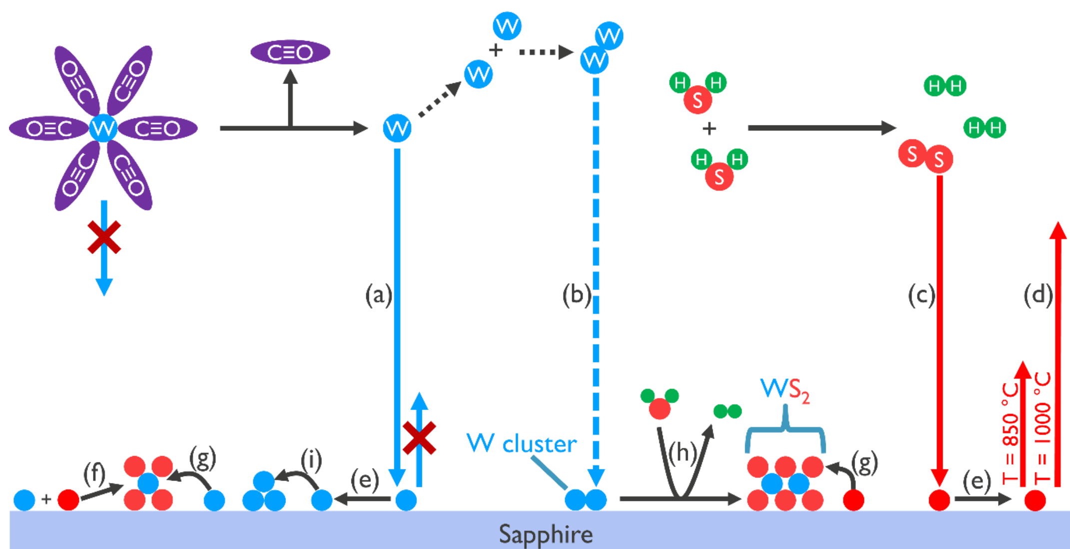

Figure 3: *Graphical representation of different processes occurring during the initial stages of WS_2 MOCVD on sapphire. The inserted precursors first undergo a series of gas phase reactions: $W(CO)_6$ dissociates into single W-atoms by removal of all carbonyl ligands and H_2S forms H_2 and S species. The liberated W-atoms can adsorb onto the sapphire surface, generating W-adatoms* ***(a)***. *Alternatively, single W-atoms can agglomerate together in the gas phase to form W clusters, which subsequently adsorb onto the sapphire surface as well* ***(b)***. *In addition, the surface also contains S adspecies following adsorption of gaseous S species* ***(c)***. *Both W- and S adspecies may desorb from the surface again, but this process is negligible for W because of its low vapor pressure. In contrast, desorption of S species significantly affects the amount of adsorbed S, and the desorption rate increases at higher temperature* ***(d).*** *The adspecies undergo a series of surface processes: they diffuse over the surface* ***(e)***, *form few-atomic WS_2 nuclei* ***(f)*** *or merge into already existing WS_2 crystals* ***(g)***. *Furthermore, adsorbed W clusters can be sulfurized into WS_2 islands* ***(h)***. *W cluster formation is not limited to the gas phase, because aggregation of single W adatoms in S-poor conditions can also result in these features* ***(i)***.

Deposition at variable temperature with intermediate anneal

In an effort to optimize the crystallinity of WS_2 while avoiding the co-deposition of metallic W, we propose a process sequence that starts with a short deposition step at 850 °C for 10 min (step I). In the next step, we remove the $W(CO)_6$ precursor from the CVD reactor and simultaneously increase the temperature to 1000 °C in the presence of H_2S. Once the temperature reaches a value of 1000 °C, we let it stabilize for an additional 5 min in the presence of H_2S (step II). During this anneal step, no WS_2 deposition can occur, but ripening and desorption may take place in addition to (reversible) adsorption of H_2S/S species and sulfurization.[17] Finally, closed MLs are formed by lateral growth of the existing nuclei/crystals by reintroducing the metal precursor into the reactor for 290 min at 1000 °C (step III). A graphical representation of this process is provided in **Figure 4a**. A similar approach using temperature variations and annealing steps was previously

demonstrated by Zhang et al.[32] (demonstrating surface diffusion processes for WSe_2 during annealing in HSe_2) and Chubarov et al. (describing increase of unidirectionality of WS_2 domains using variable-temperature deposition).[17] A comparison of the experimental conditions used in these reports and this work is provided in **Table S3**. The unique aspect in this study is the use of (0001) sapphire templates with intentional off-cut angle towards the $[1\bar{2}10]$ axis, which allows us to study both step-edge guided and crystal lattice guided epitaxy.

The process at two temperatures with intermediate annealing in H_2S ambient results only in WS_2 deposition (**Figure 4b**). Interestingly, we observe no W clusters before and after the annealing in H_2S (S1 and S2) or after 20 min of additional deposition at 1000 °C (S4, **Figure 4b**). The deposition rates at 850 and 1000 °C are equal to those observed before. The W areal density is not affected by intermediate annealing (**Figure S21**). Thus, changes in morphology due to intermediate annealing must be related to ripening effects. The absence of the W clusters in the three-step process after growth at 1000 °C (step III) suggests that intermediate annealing in H_2S has influenced the concentration and/or nature of adsorbed surface species. As discussed, the formation of W clusters may be caused by a low S versus W concentration ratio due to the fast desorption rate of S at 1000 °C. In the three-step process, WS_2 domains already partially cover the sapphire surface when starting the deposition at 1000 °C. Newly arriving W adatoms may aggregate more rapidly with existing WS_2 crystals rather than forming new W clusters. In addition, the anneal step in H_2S ambient may also result in an increased amount of adsorbed S, temporarily suppressing W co-deposition by sulfurization of W adspecies.

To understand the impact of ripening during the three-step process, we investigate the crystal number density and crystal size after each step. The initial nucleation step for 10 min at 850 °C (step I) results in WS_2 growth similar to earlier experiments at this temperature. During

intermediate annealing (step II), the crystal number density significantly decreases from 1.5 x 10^2 μm^{-2} to 5.0 x 10^1 μm^{-2} (**Figure S4**). The lower domain density combined with a similar amount of W on the surface is consistent with the lateral growth of WS_2 crystals during the anneal period. The average lateral crystal area increases from ~300 nm^2 to ~1300 nm^2 during the anneal step (**Figure 4b**). Lateral growth continues during subsequent deposition at 1000 °C (step III) for 20 min, as the crystal density remains constant while the W areal density increases (proportional to the growth rate as discussed above, **Figure S21**). Again, these observations are consistent with the AFM images, as we detect WS_2 islands with larger lateral dimensions (**Figure 4b**). The crystals grow to an average lateral area of ~2700 nm^2 during these 20 min of deposition at 1000 °C.

The crystal in-plane orientation is affected by each of the steps in the three-step process. Remarkably, the predominant orientation of the WS_2 crystals changes during the H_2S anneal, during the subsequent 1000 °C deposition step, and evolves further during coalescence (**Table 1**). We provide a schematic representation of the WS_2 crystal orientation after every deposition step in **Figure 6**. The initial growth step at 850 °C is expected to create WS_2 domains with the most favorable 0 and 60 ° orientations in addition to some intermediate oriented crystals, as described above. In contrast, after ripening during the H_2S anneal, most triangular islands have less energetically favorable 30 or 90 ° orientations (i.e., one crystal facet parallel to the direction of the step-edges, **Figure 4b** and **Figure 4c**). The 0 ° orientation becomes predominant after 20 min of additional WS_2 growth at 1000 °C, while the presence of the 30 or 90 ° options decreases slightly. We observe almost no 60 ° oriented domains at this moment (**Figure 4b** and **Figure 4c**). The crystal orientation evolves further during coalescence, favoring the most stable 0 ° and 60 ° orientations, as a closed ML consists of 54.9 % of 0 °, 43.2 % of 60 ° and 1.9 % of intermediate oriented domains (**Figure 4a**: S5, TEM analysis: **Figure 5** and **Table 1**).

In spite of the modulations in the in-plane orientation of WS_2 crystals during the individual steps, the three-step process eventually yields the highest degree of epitaxial in-plane orientation, as indicated by grazing-incidence in-plane X-ray diffraction and TEM. The recorded GIIXRD diffractograms are consistent with the findings from AFM and TEM (**Figure 5d**). Deposition at 850 °C results in a significant fraction of epitaxially oriented domains, but also a large number of crystals with other orientations. Deposition at a temperature of 1000 °C results in the disappearance of diffraction corresponding to non-epitaxial domains. The three-step deposition process results in WS_2 monolayers with an even higher degree of epitaxial in-plane orientation, as indicated by a higher signal-to-noise (S/N, +20 %) ratio and lower full-width-at-half-maximum (FWHM, -60 %) of the peak at $\varphi = 0$ ° (**Figure 5d**, **Table 1**). We observe identical trends for domain orientation when collecting electron diffraction (ED) patterns of the prepared closed ML samples on different location on each wafer (**Figure S22** – **Figure S24**). The ED patterns of the WS_2 ML deposited at 850 °C indicate all possible crystal orientations are present, whereas the patterns of MLs grown at 1000 °C or the three-step process are characteristic for crystalline WS_2 with either the 0 or 60 ° orientation. In addition, we also observe diffraction spots of the sample grown at 1000 °C (which can be related to metallic tungsten). Importantly, these additional diffraction spots are not present when analyzing the three-step process sample. Furthermore, we do not detect W particles in this ML using BF- and DF-TEM (**Figure 5a** and **Figure 5b**).

Thus, the evolution of crystal orientations during the three-step process suggests that in-plane crystal orientations can be modulated by the process conditions (**Table 1**, **Figure 6**). The mechanisms that influence the TMD domain orientation on a sapphire substrate remain under debate until now. Both the sapphire crystal lattice and surface topography have been claimed to guide the in-plane orientation of WS_2 crystals.[17–19,25–27] Interestingly, we observe WS_2 domain

orientations corresponding to epitaxial alignment (crystal lattice guided) and step-edge aligned (surface topography guided) islands at different stages of our process. Annealing in H_2S results in WS_2 domains that align with the $[10\bar{1}0]$ step-edges, and the 0 or 60 ° crystal orientation is lost. Our hypothesis about the observed changes in preferred domain orientation under variable deposition conditions is that a high amount of absorbed sulfur hinders epitaxial registry with the sapphire crystal lattice due to weaker interactions between the growing WS_2 crystal and the substrate. Under sulfur-rich conditions, e.g. after annealing in H_2S, the epitaxial registry with the sapphire crystal lattice is disturbed, leading to topography guided WS_2 domains oriented by the step-edges on the surface. A modified surface termination in S-rich conditions may lead to different formation energies of domain orientations. Aljarb et al. indeed report that the ratio between metal and chalcogen precursors plays a crucial role in the orientation of growing TMD crystals on sapphire.[51] These authors also demonstrate that MoS_2 crystals can reorient if the deposition occurs in S-rich conditions. This may be related to a high amount of adsorbed sulfur on the sapphire surface, which may lead to a weaker interaction between the growing WS_2 crystal and the sapphire epi-substrate. As a consequence, the WS_2 orientation is less guided by the substate crystal lattice, and more influenced by the surface topography. In addition, Chubarov et al. demonstrated that in S-rich conditions (higher S/W ratio compared to this study) WS_2 domains can follow the step-edge direction even when this yields non-epitaxial orientations.[17] Possibly, there exists a sort of interaction between the sapphire step-edge and the growing WS_2 domain resulting in additional stabilization, making the step-edge-aligned orientations (i.e., 30 and 90 °) energetically more favorable compared to the 0 or 60 ° orientations. A similar interaction between WSe_2 and $[1\bar{2}10]$ step-edges on sapphire (i.e., perpendicular to the step-edge direction in this study) was hypothesized by Zhu et al.[25]

The WS_2 domain orientation changes from step-edge aligned back to substrate crystal lattice guided orientation during subsequent deposition at 1000 °C. Initially, WS_2 growth at 1000 °C seems to result in the creation of islands with undefined orientation and no clear significant growth of the already present 30 and 90 ° oriented (surface topography guided) domains. However, after 20 min of deposition at 1000 °C the 0 ° orientation becomes predominant, and the step-edge aligned crystals seems to reduce in number. This observation suggests that the 0 ° (crystal lattice guided) orientation is energetically more favorable compared to step-edge alignment, and also agrees with our findings for MOCVD at a constant deposition temperature of 1000 °C. A potential explanation for the preferential formation of crystal lattice guided domains at this step of the process may be the surface termination of the sapphire surface. The amount of absorbed S species on the substrate heated at 1000 °C is significantly lower compared to the situation immediately after the H_2S anneal. Therefore, the interaction between the growing WS_2 phase and the sapphire crystal lattice is not hindered by the layer of absorbed S species. Consequently, WS_2 crystals are now guided by the epitaxial registry again instead of the weaker guiding interaction with the surface step-edges. We hypothesize that at 1000 °C WS_2 islands with the most stable orientation (i.e., the substrate crystal lattice guided options) will grow by consuming newly arriving W and S adatoms. In addition, the less energetically favorable step-edge aligned domains may dissociate into adatoms again, which also can diffuse to nearby 0 ° oriented islands. In other words, ripening can result in 0° oriented crystals growing at the expense of step-edge aligned islands. Alternatively, entire step-edge aligned WS_2 domains could reorient as a whole towards more favorable orientations. Note that reorientation of 2D domains has been reported for graphene.[52,53] Nevertheless, this would involve moving crystals across multiple step-edges (each imposing an energy barrier for atom/crystal surface diffusion). Interestingly, only the 0 ° orientation is observed

at this stage of the deposition and not the other epitaxial orientation (60 °), even though these two options are considered energetically equivalent. We cannot explain the relative occurrence of 0 ° oriented crystals versus 60 ° oriented crystals and the changes during the different process steps (**Table 1**), and this remains a topic for future research. Nevertheless, our observations illustrate the potential to tune the deposition process towards pure monocrystalline WS_2 MLs with multiple temperature steps and intermediate annealing. Furthermore, both the sapphire crystal lattice and its surface topography of the sapphire seem to guide the WS_2 orientation, and the dominating guiding factor may depend on the chemical termination of the sapphire surface.

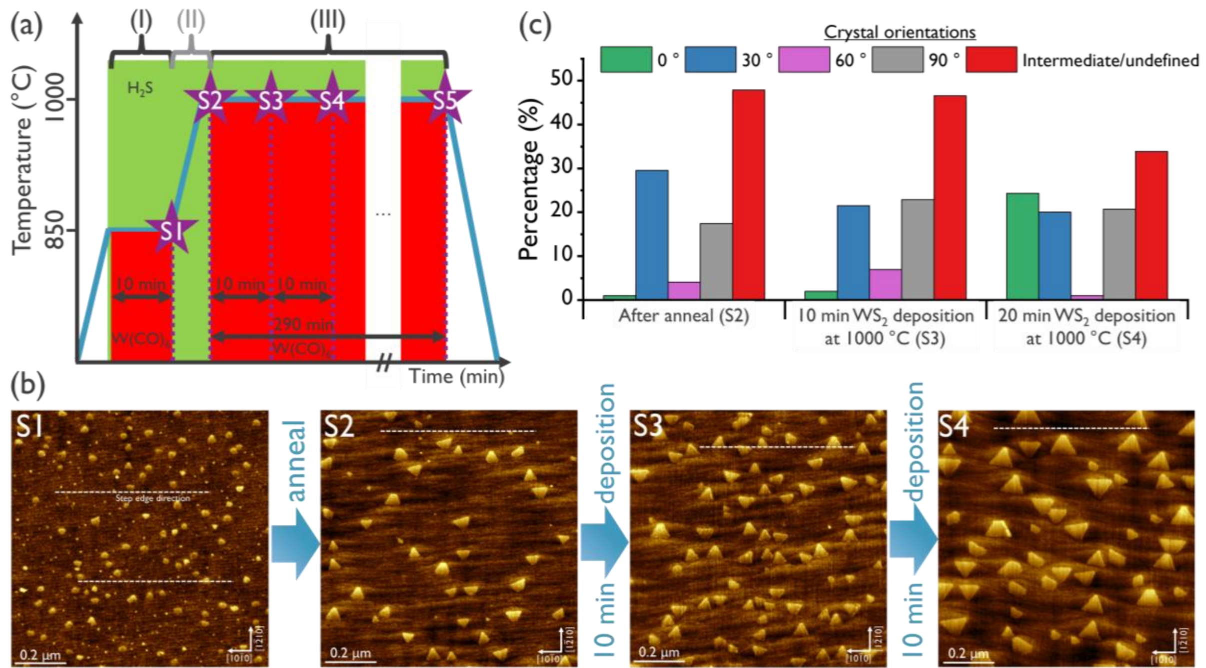

__Figure 4:__ ***(a)*** *Schematic representation of the three-step process, moments where H_2S and $W(CO)_6$ precursors are inserted are indicated by green and red, respectively. The temperature is indicated by blue line. The process consists of an initial nucleation stage with WS_2 deposition for 10 min at 850 °C (step I), followed by annealing in H_2S (step II). During this annealing period, we increase the temperature to 1000 °C and let it stabilize for an additional 5 min. Afterwards, the WS_2 deposition is resumed by reintroducing the $W(CO)_6$ into the reactor for up to 290 min (step III).* ***(b)*** *AFM topography maps at various stages of the three-step process. The sample labels (S1 to S4) correspond to different moments in the three-step process as indicated in (a).* ***(c)*** *Percentages of 0, 30, 60 and 90 ° oriented WS_2 crystals (derived from AFM topography maps in (b)). Domains with different orientations or with a shape making it impossible to assess the orientation are labelled as "intermediate/undefined".*

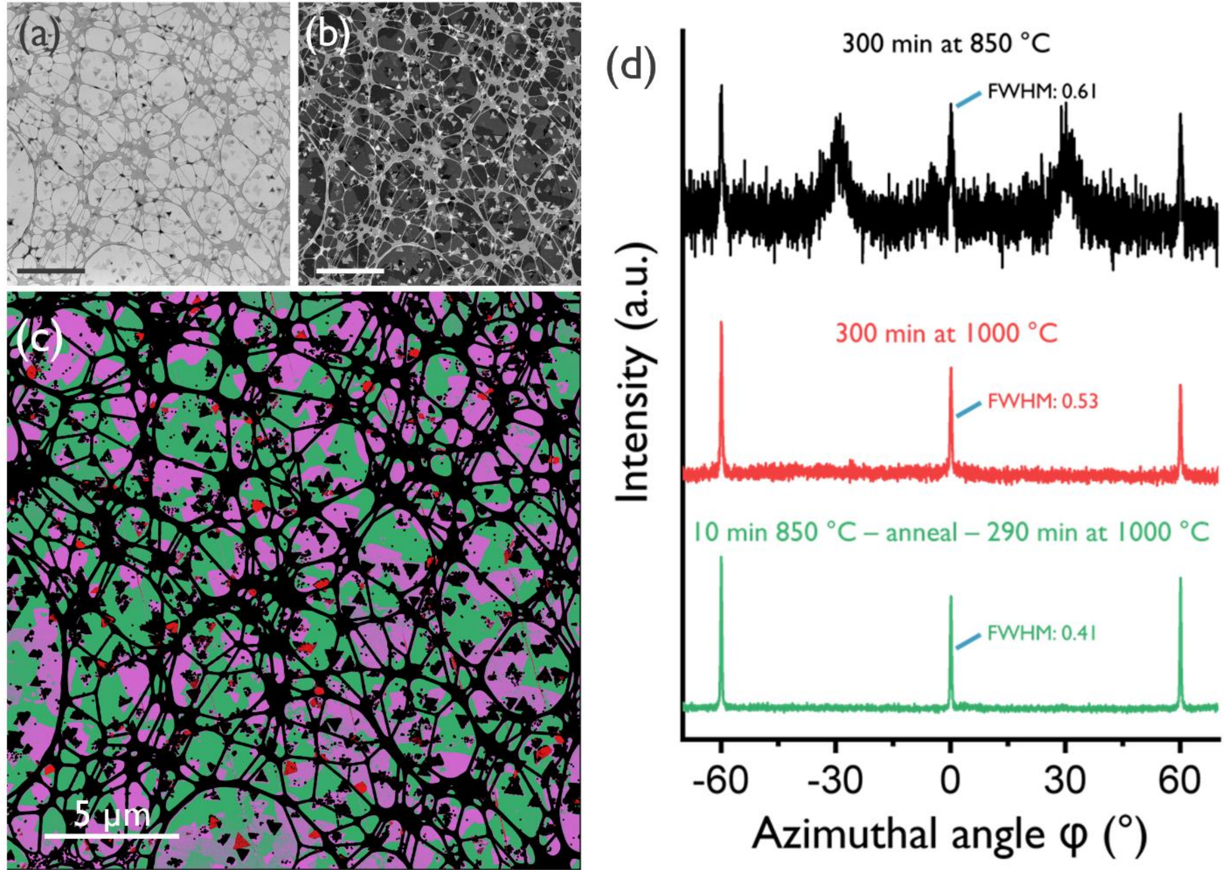

Figure 5: ***(a)*** *BF-TEM image of closed WS_2 ML obtained using the three-step process.* ***(b)*** *DF-TEM images of closed ML using the three-step process.* ***(c)*** *Segmented DF-TEM image where green corresponds to grains oriented 0°, pink to 60° and red to intermediate orientations.* ***(d)*** *GIIXRD of MLs formed at 850 °C (black) and 1000 °C (red), indicating the degree of epitaxial in-plane crystal orientations improves at higher temperature. The spectrum of the ML generated using the three-step process (green) suggests the quality of epitaxy is even higher compared processes with constant deposition temperature. The S/N ratio and FWHM of all diffractograms are provided in* ***Table 1****.*

Table 1*: Fractions of 0 °, 60 °and intermediate oriented domains after both 20 and 300 min of WS_2 deposition using a constant deposition temperature of 850 or 1000 °C or the three-step process. n.m. = not measurable.*

	After 20 min WS_2 deposition			After 300 min WS_2 deposition				
Deposition temperature (°C)	Fraction 0 ° oriented crystals (%) (AFM)	Fraction 60 ° oriented crystals (%) (AFM)	Fraction intermediate oriented crystals (%) (AFM)	Fraction 0 ° oriented crystals (%) (TEM)	Fraction 60 ° oriented crystals (%) (TEM)	Fraction intermediate oriented crystals (%) (TEM)	FWHM (°) (GIIXRD)	S/N ratio (GIIXRD)
850	n.m.	n.m.	n.m.	44.0	36.8	19.2	0.62	10
1000	41.8	23.9	34.3	61.2	29.8	8.0	0.53	36
850 - anneal - 1000	2.0	7.0	91.0	54.9	43.2	1.9	0.41	60

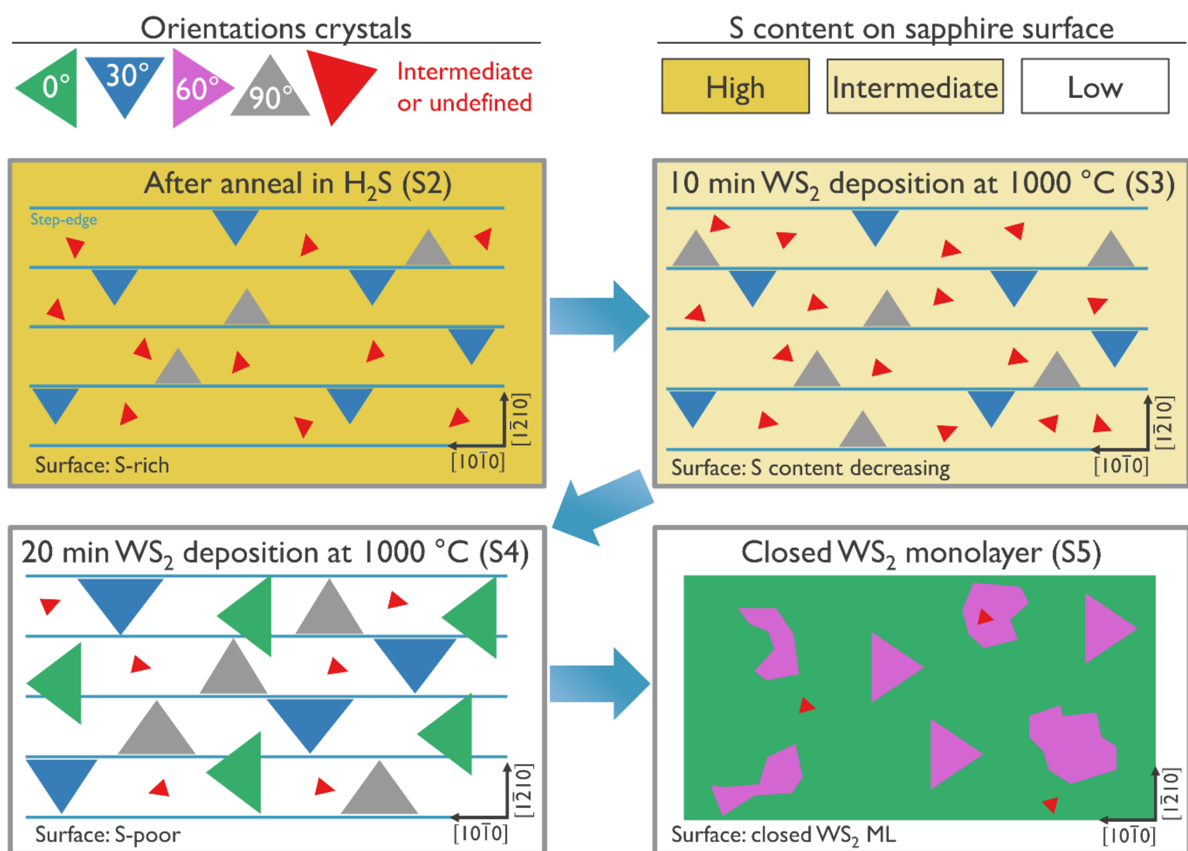

***Figure 6**: Schematic representation of WS_2 crystal orientation evolution during the three-step process. After 10 min of WS_2 deposition at 850 °C (S1) crystals do not have a clear triangular shape, making it impossible to assess the orientation. The subsequent anneal in H_2S **(S2)** leads to strong additional S adsorption onto the sapphire surface. Consequently, the epitaxial registry between WS_2 and the sapphire crystal lattice is hindered, resulting in WS_2 crystal orientation guided by the surface topography only. The amount of adsorbed S gradually decreases over time during subsequent WS_2 deposition at 1000 °C. The WS_2 domain orientation remains largely unaffected after 10 min of deposition **(S3)**, but after 20 min the substrate lattice guided orientation starts to become more present **(S4)**. This may be explained by the WS_2-sapphire epitaxial registry being less hindered in these S-poor conditions. Therefore, the influence of the surface topography on domain orientation reduces simultaneously. Continuing the WS_2 deposition at 1000 °C until closure of the first ML results in a continuous WS_2 layer which mainly consists of substrate lattice guided domains, with a minor presence of intermediate oriented domains and no crystals guided by the surface topography **(S5)**. The number of crystals of each orientation is representative for the presence percentages extracted from the AFM images (see also Figure 4c).*

CONCLUSIONS AND OUTLOOK:

We designed a MOCVD process for pure WS_2 MLs consisting of crystal domains with a preferred in-plane orientation on c-plane sapphire based on insight into the temperature dependence of WS_2 MOCVD (850 and 1000 °C). To promote high quality WS_2 epitaxy without W co-deposition, the process involves growth stages at two different temperatures and intermediate annealing in H_2S. This approach results in the deposition of pure WS_2 MLs almost entirely composed out of 0 ° and 60 ° oriented domains. Furthermore, we demonstrate that the preferential domain orientation can be modulated by the process conditions. Annealing in H_2S leads to step-edge aligned crystals, whereas subsequent deposition using both the W and S precursors results in the 0 and 60 ° oriented domains. The changes in preferred crystal orientation may depend on the surface termination. The 0 and 60 ° oriented domains are the energetically most favorable option as a result of the epitaxial registry between the WS_2 domains and the sapphire crystal lattice. Additional S species on the sapphire substrate may hinder the epitaxial registry, leading to 30 and 90 ° crystals resulting from alignment of the WS_2 domains with the sapphire step-edges. We demonstrate that the predominant crystal orientation can be changed by adjusting the amount of absorbed S during the deposition process. Nevertheless, several details of the mechanisms during epitaxy remain a topic for future research. For example, the relative occurrence of 0 ° oriented crystals versus 60 ° oriented crystals and their changes during the different process steps deserve further investigation. Furthermore, the role of the sapphire surface termination on the TMD crystal orientation should be studied in more detail using appropriate analytical techniques. Moreover, the co-deposition of metallic W can be investigated by performing deposition at different temperatures, using other gas flows or by performing anneal pretreatments of the sapphire growth surface. Finally, characterization of the optical and electrical properties of

WS_2 prepared using the tested processes may provide additional insights in structure-property relations and the impact of the deposition process. In this study, the template, (0001) sapphire with a 1° off-cut towards the $[1\bar{2}10]$ axis, was chosen so that the step-edge guided versus crystal lattice guided epitaxy could be distinguished. By using a template with the off-cut towards the $[10\bar{1}0]$ axis, both mechanisms could reenforce each other, an interesting outlook for further development.

ASSOCIATED CONTENT

The supplementary information contains additional data about samples early nucleation stage: areal density of W, crystal number density, AFM topography maps and PSD. Furthermore, Raman spectra, PL spectra and ED patterns of closed ML samples and illustrations of the experimental setup are provided. Moreover, additional WS_2 deposition experiments on annealed sapphire substrates or using a different deposition temperature and the subsequent characterization (AFM, RBS and x-ray photoelectron spectroscopy) are discussed.

AUTHOR INFORMATION

Corresponding Author

Correspondence should be addressed to J. Verdin (Joris.Verdin@imec.be), H. Medina (Henry.MedinaSilva@imec.be) and A. Delabie (Annelies.Delabie@imec.be).

Author Contributions

The manuscript was written through contributions of all authors. All authors have given approval to the final version of the manuscript.

Funding Sources

This work is part of the imec IIAP core CMOS programs and received funding from the European Union's Graphene Flagship grant agreement No 952792, 2D-EPL. I.K. acknowledges funding from the Research Foundation−Flanders for a Ph.D. fellowship strategic basic research (Project No. 1S60023N).

Notes

The authors declare no competing financial interest.

ACKNOWLEDGMENT

We would like to acknowledge Johan Desmet and Johan Meersschaut for performing RBS measurements of our samples. We also would like to thank Anja Vanleenhove and Thierry Conard for the help with x-ray photoelectron spectroscopy.

REFERENCES

(1) Chhowalla, M.; Shin, H. S.; Eda, G.; Li, L.-J.; Loh, K. P.; Zhang, H. The Chemistry of Two-Dimensional Layered Transition Metal Dichalcogenide Nanosheets. *Nat. Chem.* **2013**, *5* (4), 263–275.

(2) Lv, R.; Robinson, J. A.; Schaak, R. E.; Sun, D.; Sun, Y.; Mallouk, T. E.; Terrones, M. Transition Metal Dichalcogenides and Beyond: Synthesis, Properties, and Applications of Single- and Few-Layer Nanosheets. *Acc. Chem. Res.* **2015**, *48* (1), 56–64.

(3) Choi, W.; Choudhary, N.; Han, G. H.; Park, J.; Akinwande, D.; Lee, Y. H. Recent Development of Two-Dimensional Transition Metal Dichalcogenides and Their Applications. *Mater. Today* **2017**, *20* (3), 116–130.

(4) Akinwande, D.; Huyghebaert, C.; Wang, C.-H.; Serna, M. I.; Goossens, S.; Li, L.-J.; Wong, H.-S. P.; Koppens, F. H. L. Graphene and Two-Dimensional Materials for Silicon Technology. *Nature* **2019**, *573* (7775), 507–518.

(5) Liu, Y.; Duan, X.; Shin, H.-J.; Park, S.; Huang, Y.; Duan, X. Promises and Prospects of Two-Dimensional Transistors. *Nature* **2021**, *591* (7848), 43–53.

(6) Sebastian, A.; Pendurthi, R.; Choudhury, T. H.; Redwing, J. M.; Das, S. Benchmarking Monolayer MoS2 and WS2 Field-Effect Transistors. *Nat. Commun.* **2021**, *12* (1), 693.

(7) Fan, Y.; Zhou, Y.; Wang, X.; Tan, H.; Rong, Y.; Warner, J. H. Photoinduced Schottky Barrier Lowering in 2D Monolayer WS2 Photodetectors. *Adv. Opt. Mater.* **2016**, *4* (10), 1573–1581.

(8) Cong, C.; Shang, J.; Wang, Y.; Yu, T. Optical Properties of 2D Semiconductor WS2. *Adv. Opt. Mater.* **2018**, *6* (1), 1700767.

(9) Lan, C.; Li, C.; Ho, J. C.; Liu, Y. 2D WS2: From Vapor Phase Synthesis to Device Applications. *Adv. Electron. Mater.* **2021**, *7* (7), 2000688.

(10) Sheng, Y.; Chen, T.; Lu, Y.; Chang, R.-J.; Sinha, S.; Warner, J. H. High-Performance WS2 Monolayer Light-Emitting Tunneling Devices Using 2D Materials Grown by Chemical Vapor Deposition. *ACS Nano* **2019**, *13* (4), 4530–4537.
(11) Ago, H.; Fukamachi, S.; Endo, H.; Solís-Fernández, P.; Mohamad Yunus, R.; Uchida, Y.; Panchal, V.; Kazakova, O.; Tsuji, M. Visualization of Grain Structure and Boundaries of Polycrystalline Graphene and Two-Dimensional Materials by Epitaxial Growth of Transition Metal Dichalcogenides. *ACS Nano* **2016**, *10* (3), 3233–3240.
(12) Bao, W.; Borys, N. J.; Ko, C.; Suh, J.; Fan, W.; Thron, A.; Zhang, Y.; Buyanin, A.; Zhang, J.; Cabrini, S.; Ashby, P. D.; Weber-Bargioni, A.; Tongay, S.; Aloni, S.; Ogletree, D. F.; Wu, J.; Salmeron, M. B.; Schuck, P. J. Visualizing Nanoscale Excitonic Relaxation Properties of Disordered Edges and Grain Boundaries in Monolayer Molybdenum Disulfide. *Nat. Commun.* **2015**, *6* (1), 7993.
(13) Ogletree, D. F.; Schuck, P. J.; Weber-Bargioni, A. F.; Borys, N. J.; Aloni, S.; Bao, W.; Barja, S.; Lee, J.; Melli, M.; Munechika, K.; Whitelam, S.; Wickenburg, S. Revealing Optical Properties of Reduced-Dimensionality Materials at Relevant Length Scales. *Adv. Mater.* **2015**, *27* (38), 5693–5719.
(14) Bogaert, K.; Liu, S.; Chesin, J.; Titow, D.; Gradečak, S.; Garaj, S. Diffusion-Mediated Synthesis of MoS2/WS2 Lateral Heterostructures. *Nano Lett.* **2016**, *16* (8), 5129–5134.
(15) Najmaei, S.; Yuan, J.; Zhang, J.; Ajayan, P.; Lou, J. Synthesis and Defect Investigation of Two-Dimensional Molybdenum Disulfide Atomic Layers. *Acc. Chem. Res.* **2015**, *48* (1), 31–40.
(16) Choudhury, T. H.; Zhang, X.; Al Balushi, Z. Y.; Chubarov, M.; Redwing, J. M. Epitaxial Growth of Two-Dimensional Layered Transition Metal Dichalcogenides. *Annu. Rev. Mater. Res.* **2020**, *50* (1), 155–177.
(17) Chubarov, M.; Choudhury, T. H.; Hickey, D. R.; Bachu, S.; Zhang, T.; Sebastian, A.; Bansal, A.; Zhu, H.; Trainor, N.; Das, S.; Terrones, M.; Alem, N.; Redwing, J. M. Wafer-Scale Epitaxial Growth of Unidirectional WS_2 Monolayers on Sapphire. *ACS Nano* **2021**, *15* (2), 2532–2541.
(18) Dumcenco, D.; Ovchinnikov, D.; Marinov, K.; Lazić, P.; Gibertini, M.; Marzari, N.; Sanchez, O. L.; Kung, Y.-C.; Krasnozhon, D.; Chen, M.-W.; Bertolazzi, S.; Gillet, P.; Fontcuberta i Morral, A.; Radenovic, A.; Kis, A. Large-Area Epitaxial Monolayer MoS2. *ACS Nano* **2015**, *9* (4), 4611–4620.
(19) Fu, J.-H.; Min, J.; Chang, C.-K.; Tseng, C.-C.; Wang, Q.; Sugisaki, H.; Li, C.; Chang, Y.-M.; Alnami, I.; Syong, W.-R.; Lin, C.; Fang, F.; Zhao, L.; Lo, T.-H.; Lai, C.-S.; Chiu, W.-S.; Jian, Z.-S.; Chang, W.-H.; Lu, Y.-J.; Shih, K.; Li, L.-J.; Wan, Y.; Shi, Y.; Tung, V. Oriented Lateral Growth of Two-Dimensional Materials on c-Plane Sapphire. *Nat. Nanotechnol.* **2023**, *18* (11), 1289–1294.
(20) Ji, Q.; Kan, M.; Zhang, Y.; Guo, Y.; Ma, D.; Shi, J.; Sun, Q.; Chen, Q.; Zhang, Y.; Liu, Z. Unravelling Orientation Distribution and Merging Behavior of Monolayer MoS2 Domains on Sapphire. *Nano Lett.* **2015**, *15* (1), 198–205.
(21) Shi, Y.; Groven, B.; Serron, J.; Wu, X.; Nalin Mehta, A.; Minj, A.; Sergeant, S.; Han, H.; Asselberghs, I.; Lin, D.; Brems, S.; Huyghebaert, C.; Morin, P.; Radu, I.; Caymax, M. Engineering Wafer-Scale Epitaxial Two-Dimensional Materials through Sapphire Template Screening for Advanced High-Performance Nanoelectronics. *ACS Nano* **2021**, *15* (6), 9482–9494.

(22) van der Zande, A. M.; Huang, P. Y.; Chenet, D. A.; Berkelbach, T. C.; You, Y.; Lee, G.-H.; Heinz, T. F.; Reichman, D. R.; Muller, D. A.; Hone, J. C. Grains and Grain Boundaries in Highly Crystalline Monolayer Molybdenum Disulphide. *Nat. Mater.* **2013**, *12* (6), 554–561.
(23) Du, L.; Yu, H.; Xie, L.; Wu, S.; Wang, S.; Lu, X.; Liao, M.; Meng, J.; Zhao, J.; Zhang, J.; Zhu, J.; Chen, P.; Wang, G.; Yang, R.; Shi, D.; Zhang, G. The Effect of Twin Grain Boundary Tuned by Temperature on the Electrical Transport Properties of Monolayer MoS2. *Crystals* **2016**, *6* (9), 115.
(24) Ly, T. H.; Perello, D. J.; Zhao, J.; Deng, Q.; Kim, H.; Han, G. H.; Chae, S. H.; Jeong, H. Y.; Lee, Y. H. Misorientation-Angle-Dependent Electrical Transport across Molybdenum Disulfide Grain Boundaries. *Nat. Commun.* **2016**, *7* (1), 10426.
(25) Zhu, H.; Nayir, N.; Choudhury, T. H.; Bansal, A.; Huet, B.; Zhang, K.; Puretzky, A. A.; Bachu, S.; York, K.; Mc Knight, T. V.; Trainor, N.; Oberoi, A.; Wang, K.; Das, S.; Makin, R. A.; Durbin, S. M.; Huang, S.; Alem, N.; Crespi, V. H.; van Duin, A. C. T.; Redwing, J. M. Step Engineering for Nucleation and Domain Orientation Control in WSe2 Epitaxy on C-Plane Sapphire. *Nat. Nanotechnol.* **2023**, *18* (11), 1295–1302.
(26) Chen, L.; Liu, B.; Ge, M.; Ma, Y.; Abbas, A. N.; Zhou, C. Step-Edge-Guided Nucleation and Growth of Aligned WSe2 on Sapphire via a Layer-over-Layer Growth Mode. *ACS Nano* **2015**, *9* (8), 8368–8375.
(27) Kang, L.; Tian, D.; Meng, L.; Du, M.; Yan, W.; Meng, Z.; Li, X. Epitaxial Growth of Highly-Aligned MoS2 on c-Plane Sapphire. *Surf. Sci.* **2022**, *720*, 122046.
(28) Kandybka, I.; Groven, B.; Medina Silva, H.; Sergeant, S.; Nalin Mehta, A.; Koylan, S.; Shi, Y.; Banerjee, S.; Morin, P.; Delabie, A. Chemical Vapor Deposition of a Single-Crystalline MoS2 Monolayer through Anisotropic 2D Crystal Growth on Stepped Sapphire Surface. *ACS Nano* **2024**, *18* (4), 3173–3186.
(29) Hwang, Y.; Shin, N. Hydrogen-Assisted Step-Edge Nucleation of MoSe2 Monolayers on Sapphire Substrates. *Nanoscale* **2019**, *11* (16), 7701–7709.
(30) Cohen, A.; Mohapatra, P. K.; Hettler, S.; Patsha, A.; Narayanachari, K. V. L. V.; Shekhter, P.; Cavin, J.; Rondinelli, J. M.; Bedzyk, M.; Dieguez, O.; Arenal, R.; Ismach, A. Tungsten Oxide Mediated Quasi-van Der Waals Epitaxy of WS2 on Sapphire. *ACS Nano* **2023**, *17* (6), 5399–5411.
(31) Suenaga, K.; Ji, H. G.; Lin, Y.-C.; Vincent, T.; Maruyama, M.; Aji, A. S.; Shiratsuchi, Y.; Ding, D.; Kawahara, K.; Okada, S.; Panchal, V.; Kazakova, O.; Hibino, H.; Suenaga, K.; Ago, H. Surface-Mediated Aligned Growth of Monolayer MoS2 and In-Plane Heterostructures with Graphene on Sapphire. *ACS Nano* **2018**, *12* (10), 10032–10044.
(32) Zhang, X.; Choudhury, T. H.; Chubarov, M.; Xiang, Y.; Jariwala, B.; Zhang, F.; Alem, N.; Wang, G.-C.; Robinson, J. A.; Redwing, J. M. Diffusion-Controlled Epitaxy of Large Area Coalesced WSe2 Monolayers on Sapphire. *Nano Lett.* **2018**, *18* (2), 1049–1056.
(33) Mortelmans, W.; Kazzi, S. E.; Mehta, A. N.; Vanhaeren, D.; Conard, T.; Meersschaut, J.; Nuytten, T.; Gendt, S. D.; Heyns, M.; Merckling, C. Peculiar Alignment and Strain of 2D WSe2 Grown by van Der Waals Epitaxy on Reconstructed Sapphire Surfaces. *Nanotechnology* **2019**, *30* (46), 465601.
(34) Cuccureddu, F.; Murphy, S.; Shvets, I. V.; Porcu, M.; Zandbergen, H. W.; Sidorov, N. S.; Bozhko, S. I. Surface Morphology of C-Plane Sapphire (α-Alumina) Produced by High Temperature Anneal. *Surf. Sci.* **2010**, *604* (15), 1294–1299.
(35) Wang, R.; Guo, D.; Xie, G.; Pan, G. Atomic Step Formation on Sapphire Surface in Ultra-Precision Manufacturing. *Sci. Rep.* **2016**, *6* (1), 29964.

(36) Nalin Mehta, A.; Mo, J.; Pourtois, G.; Dabral, A.; Groven, B.; Bender, H.; Favia, P.; Caymax, M.; Vandervorst, W. Grain-Boundary-Induced Strain and Distortion in Epitaxial Bilayer MoS2 Lattice. *J. Phys. Chem. C* **2020**, *124* (11), 6472–6478.
(37) Meersschaut, J.; Vandervorst, W. High-Throughput Ion Beam Analysis at Imec. *Nucl. Instrum. Methods Phys. Res. Sect. B Beam Interact. Mater. At.* **2017**, *406*, 25–29.
(38) Zhang, J.; Wang, F.; Shenoy, V. B.; Tang, M.; Lou, J. Towards Controlled Synthesis of 2D Crystals by Chemical Vapor Deposition (CVD). *Mater. Today* **2020**, *40*, 132–139.
(39) Pierson, H. O. *Handbook of Chemical Vapor Deposition (CVD) - Principles, Technology, and Applications*, 2nd edition.; William Andrew Inc.: New York, 1999.
(40) Usoltsev, I.; Eichler, R.; Wang, Y.; Even, J.; Yakushev, A.; Haba, H.; Asai, M.; Brand, H.; Nitto, A. D.; Düllmann, C. E.; Fangli, F.; Hartmann, W.; Huang, M.; Jäger, E.; Kaji, D.; Kanaya, J.; Kaneya, Y.; Khuyagbaatar, J.; Kindler, B.; Kratz, J. V.; Krier, J.; Kudou, Y.; Kurz, N.; Lommel, B.; Miyashita, S.; Morimoto, K.; Morita, K.; Murakami, M.; Nagame, Y.; Nitsche, H.; Ooe, K.; Sato, T. K.; Schädel, M.; Steiner, J.; Steinegger, P.; Sumita, T.; Takeyama, M.; Tanaka, K.; Toyoshima, A.; Tsukada, K.; Türler, A.; Wakabayashi, Y.; Wiehl, N.; Yamaki, S.; Qin, Z. Decomposition Studies of Group 6 Hexacarbonyl Complexes. Part 1: Production and Decomposition of Mo(CO)6 and W(CO)6: *Radiochim. Acta* **2016**, *104* (3), 141–151.
(41) Zhang, Y.; Zhang, Y.; Ji, Q.; Ju, J.; Yuan, H.; Shi, J.; Gao, T.; Ma, D.; Liu, M.; Chen, Y.; Song, X.; Hwang, H. Y.; Cui, Y.; Liu, Z. Controlled Growth of High-Quality Monolayer WS2 Layers on Sapphire and Imaging Its Grain Boundary. *ACS Nano* **2013**, *7* (10), 8963–8971.
(42) Berkdemir, A.; Gutiérrez, H. R.; Botello-Méndez, A. R.; Perea-López, N.; Elías, A. L.; Chia, C.-I.; Wang, B.; Crespi, V. H.; López-Urías, F.; Charlier, J.-C.; Terrones, H.; Terrones, M. Identification of Individual and Few Layers of WS2 Using Raman Spectroscopy. *Sci. Rep.* **2013**, *3* (1), 1755.
(43) Tokunaga, T.; Kawamoto, T.; Tanaka, K.; Nakamura, N.; Hayashi, Y.; Sasaki, K.; Kuroda, K.; Yamamoto, T. Growth and Structure Analysis of Tungsten Oxide Nanorods Using Environmental TEM. *Nanoscale Res. Lett.* **2012**, *7* (1), 85.
(44) Eichfeld, S. M.; Hossain, L.; Lin, Y.-C.; Piasecki, A. F.; Kupp, B.; Birdwell, A. G.; Burke, R. A.; Lu, N.; Peng, X.; Li, J.; Azcatl, A.; McDonnell, S.; Wallace, R. M.; Kim, M. J.; Mayer, T. S.; Redwing, J. M.; Robinson, J. A. Highly Scalable, Atomically Thin WSe2 Grown via Metal–Organic Chemical Vapor Deposition. *ACS Nano* **2015**, *9* (2), 2080–2087.
(45) Ohring, M. *Materials Science of Thin Films - Deposition and Structure*, 2nd Edition.; Academic Press: San Diego, 2002.
(46) Rau, H.; Kutty, T. R. N.; Guedes de Carvalho, J. R. F. High Temperature Saturated Vapour Pressure of Sulphur and the Estimation of Its Critical Quantities. *J. Chem. Thermodyn.* **1973**, *5* (2), 291–302.
(47) *NIST-JANAF Thermochemical Tables - NIST Standard Reference Database 13*. National Institute of Standards and Technology. https://janaf.nist.gov/ (accessed 2024-06-28).
(48) Zhang, H.; van Pelt, T.; Mehta, A. N.; Bender, H.; Radu, I.; Caymax, M.; Vandervorst, W.; Delabie, A. Nucleation and Growth Mechanism of 2D SnS2 by Chemical Vapor Deposition: Initial 3D Growth Followed by 2D Lateral Growth. *2D Mater.* **2018**, *5* (3), 035006.
(49) Choi, B. J.; Choi, S.; Eom, T.; Ryu, S. W.; Cho, D.-Y.; Heo, J.; Kim, H. J.; Hwang, C. S.; Kim, Y. J.; Hong, S. K. Influence of Substrates on the Nucleation and Growth Behaviors of

Ge2Sb2Te5 Films by Combined Plasma-Enhanced Atomic Layer and Chemical Vapor Deposition. *Chem. Mater.* **2009**, *21* (12), 2386–2396.
(50) Delabie, A.; Puurunen, R. L.; Brijs, B.; Caymax, M.; Conard, T.; Onsia, B.; Richard, O.; Vandervorst, W.; Zhao, C.; Heyns, M. M.; Meuris, M.; Viitanen, M. M.; Brongersma, H. H.; de Ridder, M.; Goncharova, L. V.; Garfunkel, E.; Gustafsson, T.; Tsai, W. Atomic Layer Deposition of Hafnium Oxide on Germanium Substrates. *J. Appl. Phys.* **2005**, *97* (6), 064104.
(51) Aljarb, A.; Cao, Z.; Tang, H.-L.; Huang, J.-K.; Li, M.; Hu, W.; Cavallo, L.; Li, L.-J. Substrate Lattice-Guided Seed Formation Controls the Orientation of 2D Transition-Metal Dichalcogenides. *ACS Nano* **2017**, *11* (9), 9215–9222.
(52) Rogge, P. C.; Thürmer, K.; Foster, M. E.; McCarty, K. F.; Dubon, O. D.; Bartelt, N. C. Real-Time Observation of Epitaxial Graphene Domain Reorientation. *Nat. Commun.* **2015**, *6* (1), 6880.
(53) Woods, C. R.; Withers, F.; Zhu, M. J.; Cao, Y.; Yu, G.; Kozikov, A.; Ben Shalom, M.; Morozov, S. V.; van Wijk, M. M.; Fasolino, A.; Katsnelson, M. I.; Watanabe, K.; Taniguchi, T.; Geim, A. K.; Mishchenko, A.; Novoselov, K. S. Macroscopic Self-Reorientation of Interacting Two-Dimensional Crystals. *Nat. Commun.* **2016**, *7* (1), 10800.

****

For Table of Contents Use Only